Original research article

# Elastic, electronic and optical properties of cubic Mg$_2$C under hydrostatic pressure: Modified Becke–Johnson calculations

Jaafar Jalilian [a,*], Mosayeb Naseri [b]

[a] Young Researchers and Elite Club, Kermanshah Branch, Islamic Azad University, P.O. Box 67149-67346, Kermanshah, Iran
[b] Department of Physics, Kermanshah Branch, Islamic Azad University, Kermanshah, Iran

## ARTICLE INFO

## ABSTRACT

Using first principles calculations, structural, electronic, elastic and optical properties of Mg$_2$C crystal have been studied in the cubic phase. Elastic results presented a brittle manner for this compound. Modified Becke–Johnson correction on electronic calculations is performed to gain the correct results, and the exerting hydrostatic pressure causes to increasing energy gap as the gap direction remains from $\Gamma$ to $X$ in considered ranges of pressure. Also, the optical spectra have a blue shift to higher energies by exerting pressure. The obtained results exhibit that electronic and optical properties of Mg$_2$C crystal can be tuned by applying hydrostatic pressure.

© 2017 Elsevier GmbH. All rights reserved.

## 1. Introduction

Carbides compounds have been seriously considered from both fundamental and applied perspectives in recent decades. Recently, alkali and alkaline earth metal carbides have received investigations in advanced functional materials [1–4]. Among them magnesium carbide, as one of the common alkaline earth metal carbide containing Mg—C and C—C bonds is quite interesting from both theoretical and experimental perspectives. There are four well known magnesium carbides: (1) tetragonal MgC$_2$, (2) orthorhombic $\alpha$-Mg$_2$C$_3$, (3) monoclinic $\beta$-Mg$_2$C$_3$ and (4) cubic Mg$_2$C. MgC$_2$ compound is a tetragonal binary carbide [5], originally prepared by Novak in 1910 by the reaction of magnesium and acetylene in which two-carbon dumbbell, with 1.215 Å C—C bond length, are aligned in the perpendicular direction of the tetragonal $c$ axis [6]. The $\alpha$-Mg$_2$C$_3$ is an orthorhombic magnesium-carbon crystal which can be used as hydrogen storage materials [7,8]. The $\beta$-Mg$_2$C$_3$ is a monoclinic magnesium carbide has been recently synthesized [8]. Finally, the cubic Mg$_2$C was predicted in 1993 by Corkill and Cohen [9] and it has been recently obtained by Kurakevych et al. under high-pressure conditions [10]. It has been reported that this compound remains stable on the anti-fluorite structure (space group Fm3m, no. 225) with lattice parameter $a = 5.45$ Å at ambient pressure [11]. Furthermore, it has been shown that Mg$_2$C is a narrow band gap semiconductor with large elastic modulus [12]. Hence it is promising as a possible material for high pressure and temperature. In this paper, using first principles calculations, structural, electronic, elastic and optical properties of Mg$_2$C crystal have been studied in the cubic phase. The paper is organized as follows: the computational details are given in the next section. The results of the study, including structural properties, electronic properties and optical properties of the considered compound is presented and discussed in Section 3. Finally, the conclusion is given in the last section.

---

* Corresponding author.
  E-mail address: jaafarjalilian@gmail.com (J. Jalilian).

## 2. Computational details

Electronic and optical properties of cubic $Mg_2C$ crystal have been studied under hydrostatic pressure using first principles calculations in the framework of the density functional theory. All calculations were performed fully relativistic using WIEN2k simulation package [13]. The Kohn–Sham wave function was expanded using full potential linear augmented plane waves plus local orbital (FP-LAPW+lo) scheme. The maximum $l$ value, angular momentum, for the expansion of the wave functions in the spherical harmonics inside the Muffin-Tin spheres was set to $l_{max} = 10$, while for the expansion of the wave functions in the interstitial region, the plane-wave cutoff parameter $K_{max} = 8/R_{min}^{MT}$ was used in all calculations. Also, the charge density expansion, $\rho(r) = \sum_{G}^{G_{max}} A_G e^{iG \cdot r}$, was determined by $G_{max} = 14 Ry^{1/2}$. The Brillouin zone integration was performed with the Monkhorst-pack scheme [14] using $48 \times 48 \times 48$ and $58 \times 58 \times 58$ $k$-mesh for electronic (and elastic) and optical calculations, respectively. To expand the exchange-correlation potential, the generalized gradient approximation [15] plus modified Becke–Johnson (mBJ) potential that presented by Tran and Blaha [16]:

$$U_{\chi,\sigma}^{mBJ}(\mathbf{r}) = C U_{\chi,\sigma}^{BR}(\mathbf{r}) + (3C - 2)\frac{1}{\pi}\sqrt{\frac{10 t_\sigma(\mathbf{r})}{12 \rho_\sigma(\mathbf{r})}} \tag{1}$$

where $\rho_\sigma = \frac{1}{2}\sum_{i=1}^{N_\sigma}|\psi_{i,\sigma}|^2$ defined electron density, $t_\sigma = \frac{1}{2}\sum_{i=1}^{N_\sigma}(\nabla\psi_{i,\sigma}^*)\cdot(\nabla\psi_{i,\sigma})$ presented kinetic energy density and

$$U_{\chi,\sigma}^{BR}(\mathbf{r}) = -\frac{1}{b_\sigma(\mathbf{r})}\left(1 - e^{-\chi_\sigma(\mathbf{r})} - \frac{1}{2}\chi_\sigma(\mathbf{r})e^{-\chi_\sigma(\mathbf{r})}\right) \tag{2}$$

is Becke–Russel potential [17]. $\chi_\sigma$ quantity gain from a nonlinear equation including $\rho_\sigma$, $\nabla\rho_\sigma$, $\nabla^2\rho_\sigma$ and $t_\sigma$. Also, $b_\sigma$ can be achieved from $b_\sigma = [\chi_\sigma^3 e^{-\chi_\sigma}/8\pi\rho_\sigma]$. Another quantity, $C$ is defied as

$$C = a + b\left(\frac{1}{V_{unit-cell}}\int_{cell}\frac{|\nabla\rho(\mathbf{r}')|}{\rho(\mathbf{r}')}d^3r'\right)^{1/2} \tag{3}$$

where $a$ and $b$ are two free parameters, $a = -0.012$ (dimensionless) and $b = 1.023$ bohr$^{1/2}$. In optical section, random phase approximation (RPA) [18] has been used to calculate imaginary part of dielectric function in our optical calculations. Also, the convergence criteria was applied within charge density tolerance $|\rho_{i+1} - \rho_i| \leq 10^{-5}e$.

## 3. Results and discussion

### 3.1. Structural

The equilibrium structural parameters such as lattice constants and bulk modulus are calculated by optimizing total energy of system versus different unit cell volume. The Brich–Murnugan equation of states has been used to perform this calculations [19]:

$$E(V) = E_0 + \frac{9B_0V_0}{16}\left\{\left[\left(\frac{V_0}{V}\right)^{2/3} - 1\right]^3 B_0'\right\} + \frac{9B_0V_0}{16}\left\{\left[\left(\frac{V_0}{V}\right)^{2/3} - 1\right]^2\left[6 - 4\left(\frac{V_0}{V}\right)^{2/3}\right]\right\} \tag{4}$$

where $V_0$ is the initial considered volume, $V$ is the deformed volume, $B_0$ is the bulk modulus, and $B_0'$ is the derivative of the bulk modulus with respect to pressure. The obtained structural parameters are summarized in Table 1 compared with previous calculations. Our results have a good consistency with the other experimental computational values. Fig. 1a illustrates the variation of the total energy versus unit cell volume. According to Brich–Murnagan equation, the correct equilibrium volume achieve when the $E$–$V$ curve has a perfect parabolic shape and this curve had been calculated for different volume close to equilibrium volume. Since the other structural parameters have been derived from this figure such as bulk modulus ($B_0$) and its derivation ($B_0'$), so this part of calculations has a main role in characterizing structural and elastic properties of materials. The variation of cell volume against pressure has been performed for both Murnagan and Brich–Murnagan equation states (see Fig. 1b). As it can be seen from this figure, both fitting equation has a good similarity around equilibrium, but the curves experience different values in high range of pressure (see inset picture in Fig. 1b). Therefore, a similar behavior to fit pressure–volume curve has been concluded in low pressure ranges.

**Table 1**
Calculated structural and elastic parameters in this work and compared with previous calculations.

| | a (Å) | $B_0$ (GPa) | $B_0 = \frac{C_{11}+2C_{12}}{3}$ (GPa) | $B_0'$ | $C_{11}$ (GPa) | $C_{12}$ (GPa) | $C_{44}$ (GPa) |
|---|---|---|---|---|---|---|---|
| This work | 5.445 | 90.57 | 91.2 | 3.94 | 276.3 | −1.3 | 55.2 |
| Ref. [12] | 5.36 | 104.5 | 102.75 | 3.93 | 268.76 | 19.74 | 106.44 |
| Ref. [11] | 5.36 | 104.7 | – | 3.54 | – | – | – |
| Ref. [20] | 5.44 | 104.7 | | 3.54 | – | – | – |
| Ref. [21] | 5.443 | 90.3 | | – | – | – | – |
| Ref. [9] | 5.448 | 91 | | 4.02 | – | – | – |
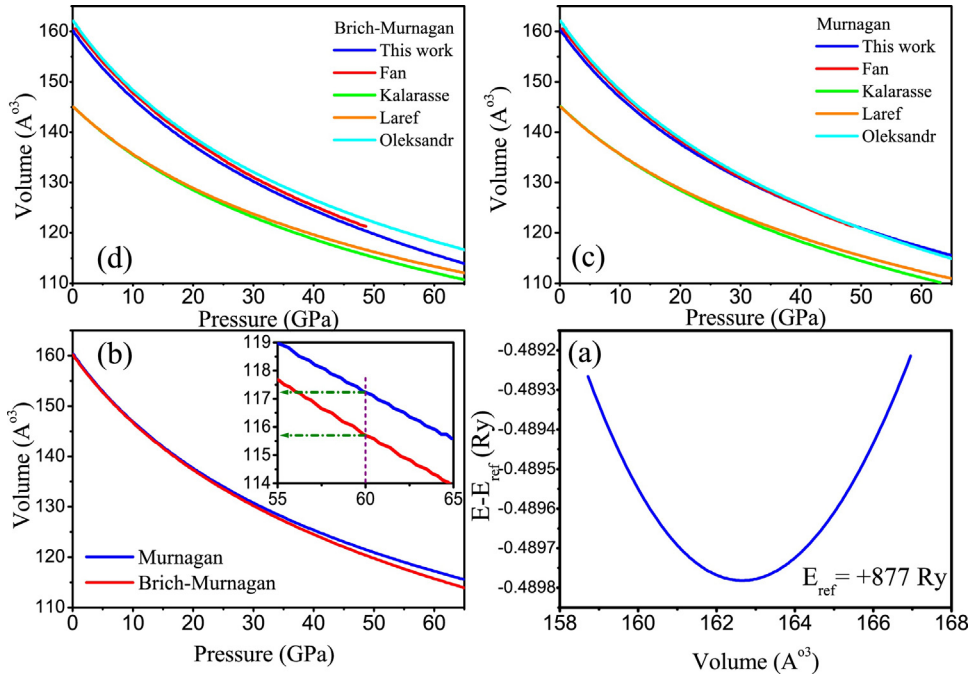
**Fig. 1.** (a) Calculated energy variation versus volume of unit cell using Brich–Murnagan equation state, (b) comparing Murnagan and Brich–Murnagan results for volume variation against applied pressure (GPa), (c) volume–pressure graphs for Murnagan scheme and (d) volume–pressure graphs for Brich–Murnagan scheme.

In the other hand, to investigate the effect of volume optimization effects on structural and elastic properties, our results are presented and compared with previous calculations for both Murnagan and Brich–Murnagan schemes. So, the volume versus pressure are calculated and plotted in Fig. 1c and d. The results expressed that our results have a good agreement with Fan et al. [20], Oleksandr et al. [9] and Kaur [21] calculations. But Laref [12] and Kalarasse et al. [11] results are different from the other calculations. As we know, a dense k-mesh is needed to achieve an acceptable accuracy in structural and elastic data. After studying computational parts of Laref and Kalarasse articles, we found that they used a low k-mesh in their calculations, $4 \times 4 \times 4$ and $10 \times 10 \times 10$, respectively. While, the present structural calculations are performed for $48 \times 48 \times 48$ k-mesh. So, their structural and elastic results do not have an acceptable accuracy to investigate elastic behavior.

### 3.2. Elastic

In this section, the elastic properties of $Mg_2C$ compound are investigated for equilibrium of pressure–volume conditions. These properties can be achieved form calculating of ground states energy of compounds. The most important parameters in this calculation are elastic constants, $C_{ij}$, which present elastic behavior of materials. Other elastic parameters can be derived from these constants such as Young and shear modulus, ductility, sound velocity, Debye temperature, etc. For cubic crystals, there are only three independent elastic constants: $C_{11}$, $C_{12}$, $C_{44}$ and their linear combination gives the value of the bulk modulus $B = (C_{11} + 2C_{12})/3$ of crystal. There is not any experimental values of elastic constants of $Mg_2C$, so we tried to calculate these parameters in a high computational accuracy.

The elastic constants of $Mg_2C$ are summarized in Table 1. As it is clear, the bulk modulus obtained from elastic constants and Brich–Murnagan equation has a good agreement that prove our calculations. Laref results have significant difference with our calculations. As it was mentioned, chosen k-mesh in elastic calculations has a effective role on obtained elastic constants. The difference between our results and Laref is related to a low k-mesh of Laref calculations. From Table 1 it can be observed that the $C_{11}$ is about five times higher than $C_{44}$ that indicates that this crystal presents a weaker resistance to shear deformation compared to the resistance to the unidirectional compression. This ratio, $C_{11} \approx 5C_{44}$, is lower than 3 times in Laref calculations.

The mechanical stability criteria for a cubic crystal are as follow [22]:

$$C_{11} - C_{12} > 0, \quad B > 0, \quad C_{44} > 0 \tag{5}$$

The results exhibit these criteria are satisfied for $Mg_2C$ crystal that suggesting it is mechanically stable. There are some elastic parameters that can help us to discuss about the elasticity of materials such as Young's modulus ($E$), Poisson's ratio ($\nu$), shear modulus, elastic anisotropy ($A$) and ductility ratio ($B/G$). According to the Voigt–Reuss–Hill approximation [23], the corresponding polycrystalline bulk modulus and shear modulus are extracted from the single crystal elastic constants,

**Table 2**
Calculated elastic parameters that are compared with other theoretical calculations.

|  | $E$ (GPa) | $G_V$ (GPa) | $G_R$ (GPa) | $G$ (GPa) | $B/G$ | $\nu$ | $A$ |
|---|---|---|---|---|---|---|---|
| This work | 187 | 88.6 | 72.7 | 80.7 | 1.13 | 0.158 | 0.4 |
| Other work (Ref. [12]) | 248.6 | 113.6 | 113 | 113.3 | 0.9 | 0.096 | 0.855 |

$C_{ij}$. Also, the other mentioned elastic quantities ($E$ and $\nu$ and $A$) can be computed from these parameters using the following relationship [24]:

$$E = \frac{9BG}{3B + G} \tag{6}$$

$$\nu = \frac{B - E}{6B} \tag{7}$$

$$A = \frac{2C_{44}}{C_{11} - C_{12}} \tag{8}$$

These values are listed and compared by Laref results in Table 2. As it is mentioned, the bulk modulus $B$ denotes resistance to fracture while the shear modulus $G$ represents resistance to plastic deformation. A $B/G$ ratio has been presented by Pugh [25] as a factor to investigate ductility or brittleness behavior of material. The critical value, which separates ductile and brittle materials is about 1.75, i.e., if $B/G > 1.75$ the compound consider as a ductile material. In contrast, materials that have $B/G$ value lower than 1.75 behave in a brittle manner. The obtained value for this ratio in our calculations is 1.13; suggesting that this compound is a brittle compound. The previous result for this quantity is about 0.9 that refers to difference in obtained shear modulus ($G$).

Another important quantity to study elastic properties of materials is Poisson's ratio ($\nu$) which provides information about the type of forces between atomic bonds in compounds. According to Haines et al. [26] scheme for pure covalent materials this parameter is small (typically 0.1), but a typical value for an ionic material is about 0.25. The obtained value for Mg$_2$C crystal is about 0.158 which suggests an ionic contribution in intra-atomic bonding for Mg$_2$C. Finally, elastic anisotropy parameter is studied by elastic constants dependency:

$$A = \frac{2C_{44}}{C_{11} - C_{12}} \tag{9}$$

The value of this parameter for an isotropic crystal is equal to 1, so any deviations from 1 indicate anisotropy which is a measure of the degree of elastic anisotropy of the crystal. Our results present $A = 0.4$ that exhibits an anisotropic behavior of elastic parameters. Two-dimensional plot of Young's modulus is illustrated in Fig. 2a in $x$–$y$ plane. This graph has an exact circle form for a perfect isotropic crystal. It is obvious that for Mg$_2$C there is an anisotropy in Young's modulus quantity in $x$–$y$ atomic plane. A better visualization of the elastic anisotropy is obtained by calculating a three-dimensional surface exhibiting dependence of the Young's modulus $E$ on a direction in a solid. For cubic crystals, such a surface is described by the following equation:

$$E(\mathbf{n}) = \frac{1}{S_{11} - \beta \left( n_1^2 n_2^2 + n_1^2 n_3^2 + n_2^2 n_3^2 \right)} \tag{10}$$

where $\beta = 2S_{11} - 2S_{12} - S_{44}$ and $S_{ij}$ are the values of elastic compliance constants (measured in GPa$^{-1}$). These parameters are gained from the inverse matrix of elastic constants matrix $C_{ij}$. Also, $n_1$, $n_2$ and $n_3$ are the direction cosines that determine the angles between $a$, $b$, $c$ axes of a crystal and a given direction. According to the mentioned equation, presented Young's modulus expresses a perfect sphere for an isotropic crystal, so it contravenes from spherical shape by increasing elastic anisotropy. As it can be seen from Fig. 2b, Young's modulus has same behavior in the $x$, $y$ and $z$ directions, but there is an anisotropy in the other directions of crystal that cause to a distortion in the spherical shape of its.

### 3.3. Electronic properties

In this section, the electronic properties of Mg$_2$C compound are investigated under hydrostatic pressure in 0–60 GPa range. Considered values of pressure are $P = 0$, 20, 40 and 60 GPa. The selection of these values refers to the value of elastic constants such as $B = 90.5$ GPa. Two-dimensional charge density distribution is illustrated in Fig. 3a–d for all systems. In free-stressed case, the charge overlap between carbon and magnesium atoms is not significant as the atomic charge is localized around each atoms. While the charge overlap increases by exerting pressure on system, and a rearrangement occurs for charge density distribution between Mg and C atoms. Also, the on-site charge density contribution is plotted in Fig. 3e along Mg—C—Mg bonds. As it can be seen, applying stress does not have remarkable effect of charge accumulation around both atoms, but it just changes the peak intensity of charge density. These graphs illustrate an ionic nature is stronger than covalent behavior for Mg—C bond in Mg$_2$C compound.

Electronic band structure of all systems is calculated and plotted in Fig. 4. As it can be seen from figure, Mg$_2$C compound is an indirect gap semiconductor from $\Gamma$ to $X$ direction. The results illustrate that the valence band maximum (VBM) is located
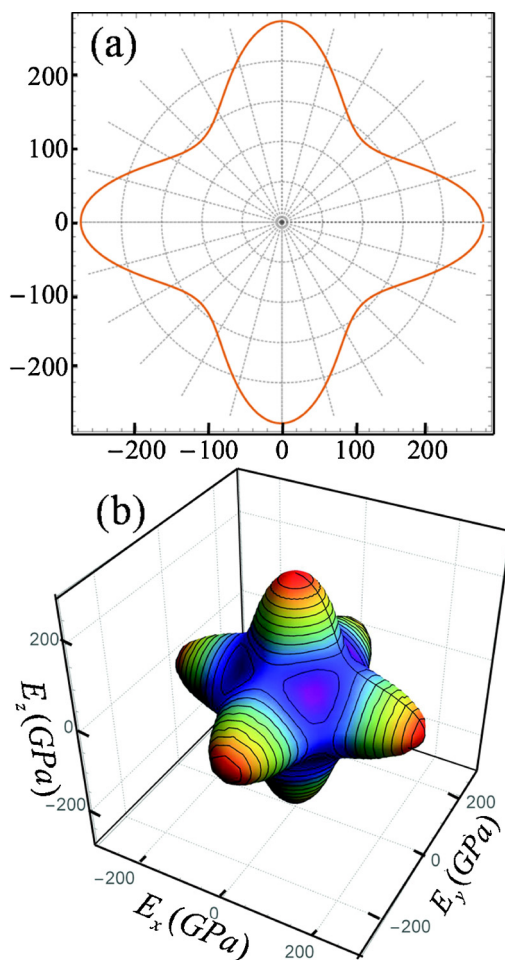
**Fig. 2.** Directional dependence of the Young's moduli of the cubic Mg$_2$C crystal based on GGA–mBJ calculations in equilibrium conditions in (a) $x$–$y$ plane and (b) three dimensional. All values are presented in GPa.

in $\Gamma$ direction for all stressed systems, so the exerting stress do not affect on VBM energy level. In other hand, the conduction band minimum (CBM) is in $X$ direction. In the conduction band, applying stress causes to shifting the energy level in $\Gamma$ direction to higher energy with respect to conduction edge in $X$ direction. By considering these variations, we can result that the energy gap of Mg$_2$C compound be direct type in strain conditions, i.e. for lattice constants higher the equilibrium ones.

Variation of energy gap versus applied pressure in our calculations is illustrated and compared with previous works (see Fig. 5). In the top panel of Fig. 5, the energy gap variation along $\Gamma$ to $X$ direction is presented. The results express that there are major differences between our calculations and previous results. Our results show that we have an increasing in energy gap about 9.5% with respect to equilibrium band gap. While Kalarasse calculations presented that the energy gap along $\Gamma$ to $X$ direction do not have a significant variation and approximately it has a fixed value. Also, Li results exhibit a different behavior in comparison with our calculations. They showed that the energy gap value decreases by increasing applied pressure. In both calculations, Kalarasse and Li results, they used local density approximation to expand exchange-correlation functional. As we know, this functional could not present a good description of exchange-correlation effects and there is an underestimation in energy gap by this functional. As it has been mentioned, the modified Becke–Johnson functional is used in our calculation to gain correct results for energy band gap. In low panel of Fig. 5, the variation of band gap along $\Gamma$ to $\Gamma$ is illustrated. By comparing our results and Kalarasse results, we can see that both results have similar behavior as the energy gap increases by increasing pressure. The difference in gap values refers to using different exchange-correlation functionals.

### 3.4. Optical properties

Studying optical properties of materials help us to suggest optoelectronic applications for them. Calculating complex dielectric function, $\varepsilon = \varepsilon_1 + i\varepsilon_2$, is the first step of optical investigation. In this article, the imaginary part of dielectric function
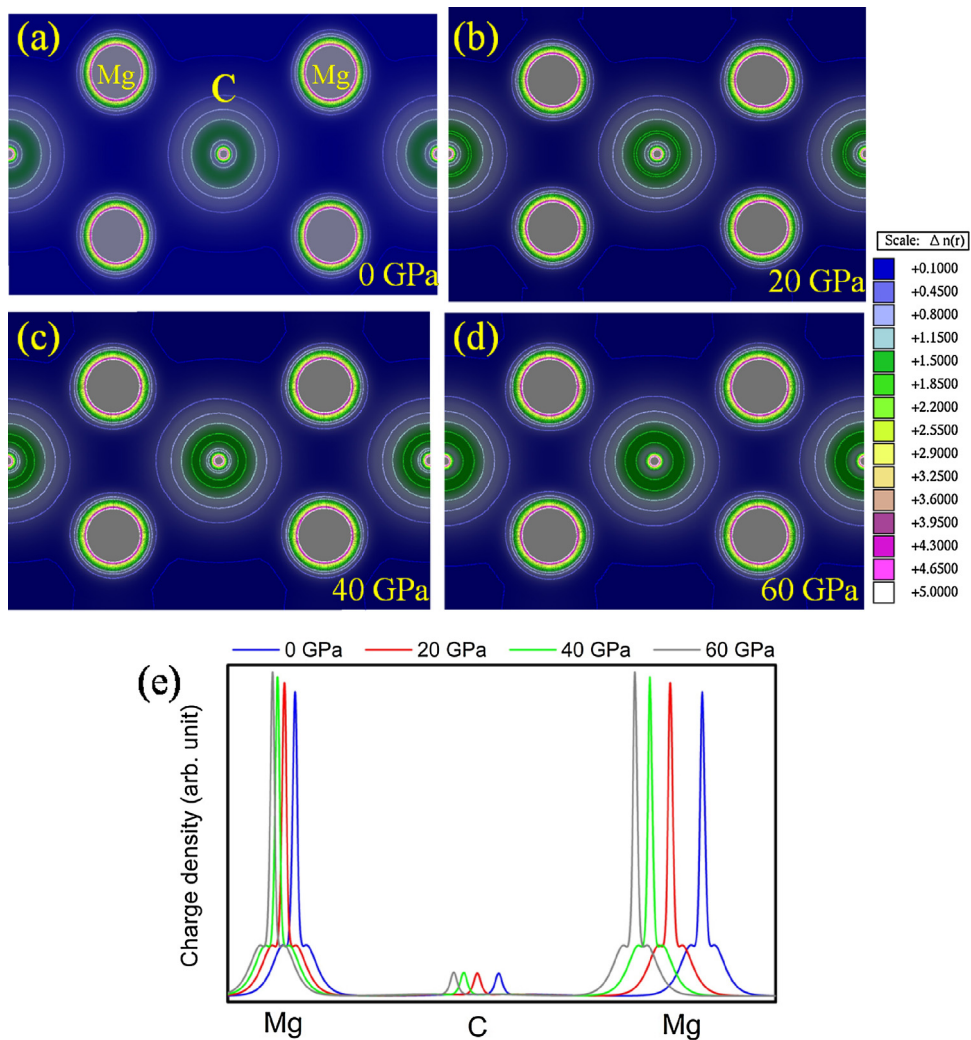
**Fig. 3.** Two-dimensional charge density distribution in (011) plane for (a) $P = 0$, (b) $P = 20$, (c) $P = 40$ and (d) $P = 60$ GPa. (e) On-site charge density of valence electron along Mg—C—Mg bond.

in derived from random phase approximation (RPA) scheme. Also, using Kramers-Kronig relations, the real part of dielectric function can be obtained from imaginary part.
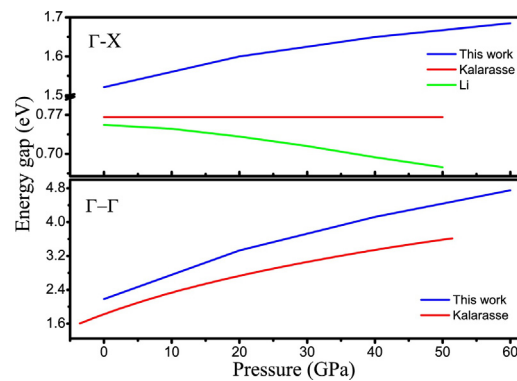
The imaginary part of dielectric function is plotted for equilibrium system and under hydrostatic pressure condition in Fig. 6. Existing a threshold in this peak refers to semiconducting properties of systems. It is obvious that there are two main peaks in each spectrum that they have a blue shift by increasing hydrostatic pressure. This spectrum has a direct relation with optical absorption spectrum that is related to electron transition from valence band to conduction band by absorbing energy of incident photon. Similar to imaginary part, the optical absorption spectrum has a blue shift by exerting pressure. The inset picture in Fig. 7 illustrates that the threshold of optical absorption spectrum moves towards higher energies by increasing pressure, and this spectrum reach to a zero value up to 25 eV.

To discuss about optical transitions, the joint density of states (JDOS) is calculated that refer to optical interband transitions from valence band to conduction band (see Fig. 8). Threshold of JDOS expresses the optical gap that is the first transition from valence to conduction band. The sharp peaks in this graph refer to degenerate transitions in energy band structure. The first main peak in this graph has a sharp behavior that moves toward higher energies by increasing pressure. As it is clear, the threshold shape of spectrum in zero pressure is different from other cases that are under hydrostatic pressure.

The other optical spectrum that is discussed is real part of dielectric function. The real part spectrum obtained in our calculations is compared with Laref results in Fig. 9a. As it can be seen, the general shape of spectra is similar to each other, but there are some difference in magnitude and peak positions that they refer to using different exchange-correlation terms. The static dielectric constant, $\varepsilon_1(0)$, versus applied pressure is plotted and compared by Li and Kalarasse calculations in Fig. 9b. It is obvious that variation of $\varepsilon_1(0)$ against pressure in our calculations has a softer trend in comparison with other results. Also, our results (blue line) present smaller values with respect to Li and Kalarasse spectra. As we mentioned, they
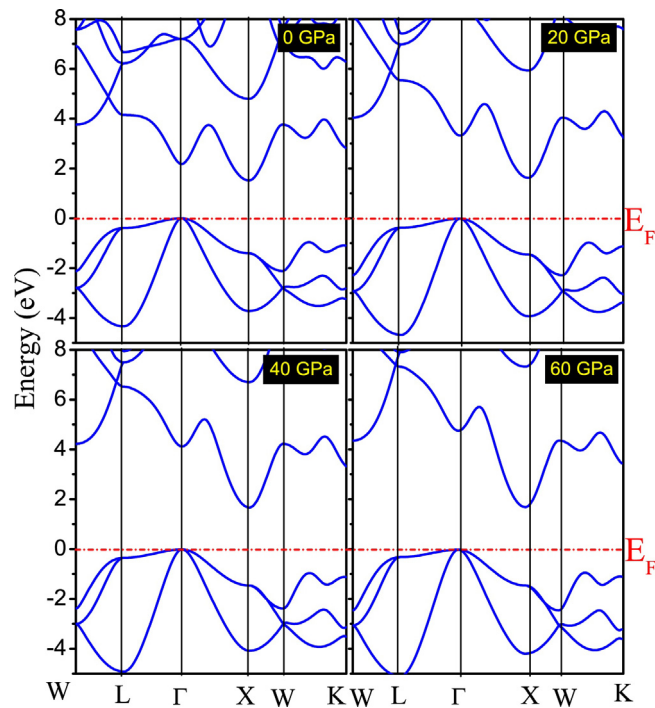
**Fig. 4.** Calculated energy band structure for all systems by GGA–mBJ functional. The dashed red line denotes to the Fermi energy at zero. (For interpretation of the references to color in this figure legend, the reader is referred to the web version of the article.)
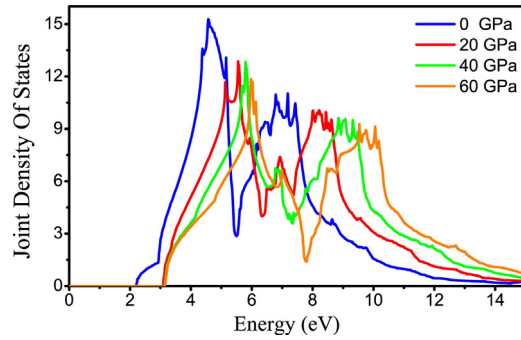


**Fig. 5.** Variation of energy band gap for indirect gap (top panel) $\Gamma \to X$ and direct gap (low panel) $\Gamma \to \Gamma$.
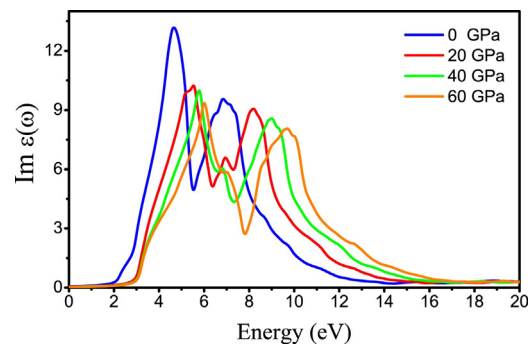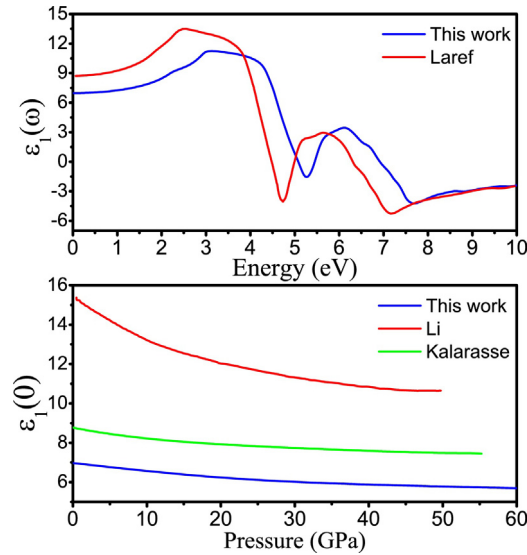


**Fig. 6.** Imaginary part of dielectric function versus incident photon energy.
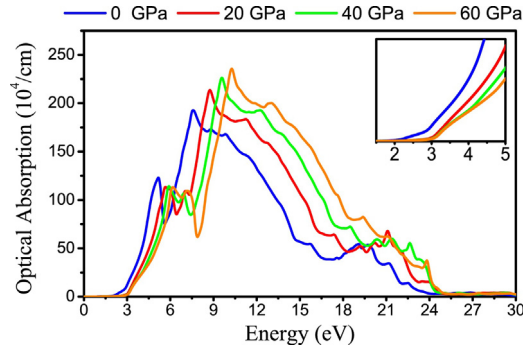
**Fig. 7.** Calculated optical absorption spectrum for all cases. The inset figure clarify the threshold of all spectra.



**Fig. 8.** Joint density of states to investigate optical interband transitions.



**Fig. 9.** (a) Comparing the obtained real dielectric function in this work by other previous calculation. (b) Pressure dependency of static dielectric function in present work by different calculations.

used LDA functional in their calculations that it leads to a underestimation in the energy gap value. While in the present study, we used GGA–mBJ functional that shows a good accuracy about this calculations. On other hand, we checked these results by Penn model [27] about the relation between static dielectric function and energy gap of semiconductor materials:

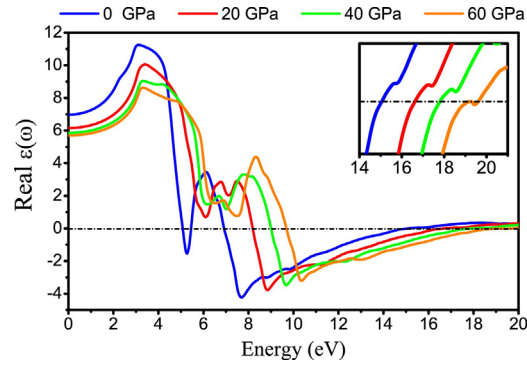$$\varepsilon_1(0) = 1 + \left( \frac{\hbar}{E_g} \right)^2 \tag{11}$$

**Fig. 10.** Real part of dielectric function versus photon energy for all considered pressure.
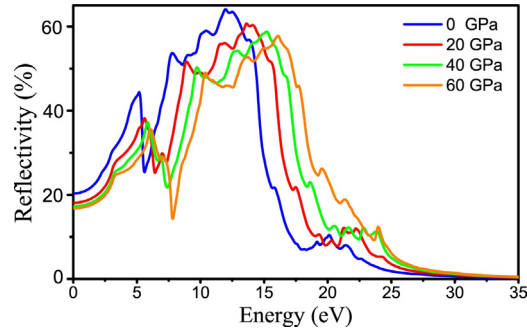


**Fig. 11.** Reflectivity spectrum in percent for all cases.

It is clear that the larger band gap results in a smaller static dielectric constant, so difference between our results and previous works refers to energy band gap calculations. Fig. 10 illustrates the real part of dielectric function versus pressure in GPa. Applied pressure causes to shifting spectra to higher energies (blue shift). Real part and reflectivity spectrum are related to each others:

$$R(\omega) = \left| \frac{\sqrt{\varepsilon(\omega)} - 1}{\sqrt{\varepsilon(\omega)} + 1} \right|^2 \tag{12}$$

The reflectivity spectrum has a large value when the real part of dielectric function is negative (see Fig. 11). The reflectivity spectrum expresses a reflectance about 20% in visible range of light, and this percent decreases by increasing hydrostatic pressure. Obviously, Mg$_2$C has a transparent behavior up to energy about 25 eV that this spectrum reaches zero value. Another spectrum that has a tight relation with real part of dielectric function is the electron energy loss function (ELOSS)
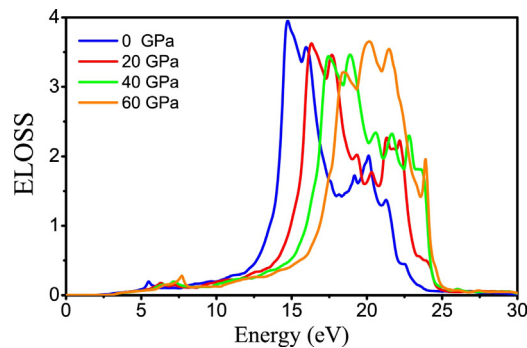


**Fig. 12.** Electron energy loss function of Mg$_2$C under hydrostatic pressure.

which describes the energy is lost by a fast moving electron travelling throughout the material [28]. The energy loss function that is calculated directly from the total dielectric function as:

$$L(\omega) = \frac{\varepsilon_2(\omega)}{\varepsilon_1^2(\omega) + \varepsilon_2^2(\omega)} \tag{13}$$

As we know, the most prominent peak in the ELOSS is identified as the plasmon peak, signaling the energy of collective excitations of the electronic charge density in the materials (see Fig. 12). On other hand, $\varepsilon_1(\omega) = 1 - (\omega_p^2/\omega^2)$, so the roots of real part denote to plasma frequency of compound. By comparing the main peaks in ELOSS and roots of real dielectric function, we can determine the plasma frequency of $Mg_2C$. The inset figure in Fig. 10 locates the value of plasma frequency for all compounds. This quantity for equilibrium system is about 15 eV, so it moves toward higher energies by increasing pressure.

## 4. Conclusion

Structural, elastic, electronic and optical properties of cubic $Mg_2C$ crystal performed were performed using fist principles calculation under hydrostatic pressure. The obtained results were calculated using modified Becke–Johnson correction to gain accurate information about semiconducting properties of crystal under pressure. The results exhibited that this crystal is an indirect type semiconductor that the energy gap increases by increasing pressure. All obtained results were compared by other theoretical and experimental calculations. Elastic results demonstrated that this compound has a brittle manner and there is an anisotropy in elastic quantities. Also, exerting hydrostatic pressure cause to a blue shift in optical spectra. The plasma frequency of $Mg_2C$ has soft increasing to higher energies by increasing applied pressure. All obtained results persuade us to suggest new optoelectronic application for cubic $Mg_2C$ crystal under hydrostatic pressure conditions.

## Acknowledgements

## References

[1] M. Atoji, R.C. Medrud, Structures of calcium dicarbide and uranium dicarbide by neutron diffraction, J. Chem. Phys. 31 (1959) 332–337.
[2] O. Reckeweg, A. Baumann, H.A. Mayer, J. Glaser, H.J. Meyer, Über die Koexistenz von tetragonalem und monoklinem $CaC_2$: Strukturelle und spektroskopische Untersuchungen an Erdalkalimetallacetyliden, $MC_2$ (M = Ca, Sr, Ba), Z. Anorg. Allg. Chem. 625 (1999) 1686–1692.
[3] U. Ruschewitz, Binary and ternary carbides of alkali and alkaline-earth metals, Coord. Chem. Rev. 244 (2003) 115–136.
[4] A. Largo, P. Redondo, C. Barrientos, On the competition between linear and cyclic isomers in second-row dicarbides, J. Am. Chem. Soc. 126 (2004) 14611–14619.
[5] P. Karen, A. Kjekshus, Q. Huang, V.L. Karen, The crystal structure of magnesium dicarbide, J. Alloys Compd. 282 (1999) 72–75.
[6] J.Z. Novák, Phys. Chem. 73 (1910) 513.
[7] H. Fjellvaag, P. Karen, Crystal structure of magnesium sesquicarbide, Inorg. Chem. 31 (1992) 3260–3263.
[8] A. Kubota, H. Miyaoka, M. Tsubota, K. Shimoda, T. Ichikawa, Y. Kojima, Synthesis and characterization of magnesium-carbon compounds for hydrogen storage, Carbon 56 (2013) 50–55.
[9] O.O. Kurakevych, T.A. Strobel, D.Y. Kim, G.D. Cody, Synthesis of $Mg_2C$: a magnesium methanide, Angew. Chem. Int. Ed. 52 (2013) 8930–8933.
[10] O.O. Kurakevych, Y. Le Godec, T.A. Strobel, D.Y. Kim, W.A. Crichton, J. Guignard, High-pressure and high-temperature stability of antifluorite $Mg_2C$ by in situ X-ray diffraction and ab initio calculations, J. Phys. Chem. C 118 (2014) 8128–8133.
[11] F. Kalarasse, B. Bennecer, Electronic and optical properties of the antifluorite semiconductors $Be_2C$ and $Mg_2X$ (X = C, Si, Ge) under hydrostatic pressure, J. Phys. Chem. Solids 69 (2008) 1775–1781.
[12] S. Laref, A. Laref, Mechanical, electronic and optical properties of antifluorites semiconductors $X_2C$ (X = Mg, Be), Comput. Mater. Sci. 44 (2008) 664–669.
[13] P. Blaha, K. Schwarz, G.K.H. Madsen, D. Kvasnicka, J. Luitz, K. Schwarz, An augmented PlaneWave + Local Orbitals Program for calculating crystal properties revised edition WIEN2k 13.1 (release 06/26/2013) Wien2K users guide, ISBN:3-9501031-1-2.
[14] H.J. Monkhorst, J.D. Pack, Special points for Brillouin-zone integrations, Phys. Rev. B 13 (1995) 5188.
[15] J.P. Perdew, K. Burke, M. Ernzerhof, Generalized gradient approximation made simple, Phys. Rev. Lett. 77 (1996) 3865–3868.
[16] F. Tran, P. Blaha, Accurate band gaps of semiconductors and insulators with a semilocal exchange-correlation potential, Phys. Rev. Lett. 102 (2009) 226401.
[17] A.D. Becke, M.R. Roussel, Exchange holes in inhomogeneous systems: a coordinate-space model, Phys. Rev. A 39 (1989) 3761.
[18] H. Ehrenreich, M.H. Cohen, Self-consistent field approach to the many-electron problem, Phys. Rev. 115 (1959) 786–790.
[19] F. Birch, Equation of state and thermodynamic parameters of NaCl to 300 kbar in the high-temperature domain, J. Geophys. Res. B 83 (1978) 1257–1268.
[20] Ch. Fan, J. Li, First-principles investigation of novel polymorphs of $Mg_2C$, Phys. Chem. Chem. Phys. 17 (2015) 12970–12977.
[21] K. Kaur, R. Kumar, First principle investigation of the electronic and thermoelectric properties of $Mg_2C$, Chin. Phys. B 25 (2016) 026402–026405.
[22] S. Yip, J. Li, M. Tang, J. Wang, Mechanistic aspects and atomic-level consequences of elastic instabilities in homogeneous crystals, Mater. Sci. Eng. A 317 (2001) 236240.
[23] E. Schreiber, O.L. Anderson, N. Soga, Elastic Constants and Their Measurement, McGraw-Hill, New York, 1973.
[24] Sh. Soleimanpour, F. Kanjouri, Elastic, electronic and optical properties of the cubic fluoro-perovskite $KCaF_3$ under pressure, Ind. J. Phys. 89 (2015) 687–697.
[25] S.F. Pugh, Relations between the elastic moduli and the plastic properties of polycrystalline pure metals, Philos. Mag. 45 (1954) 823–843.
[26] J. Haines, J.M. Leger, G. Bocquillon, Synthesis and design of superhard materials, Annu. Rev. Mater. Res. 31 (2001) 1–23.
[27] D.R. Penn, Wave-number-dependent dielectric function of semiconductors, Phys. Rev. 128 (1962) 2093.
[28] S. Naderizadeh, S.M. Elahi, M.R. Abolhassani, F. Kanjouri, N. Rahimi, J. Jalilian, Electronic and optical properties of Full-Heusler alloy $Fe_{3-x}Mn_xSi$, Eur. Phys. J. B 85 (2012) 144–151.